

Magnetic Nanostructures Produced By Electron Beam Patterning Of Direct Write Transition

Metal Fluoride Resists

Dmitry Streblechenko and M.R. Scheinfein

Department of Physics and Astronomy, PSF-470 Box 871504, Arizona State University,

Tempe, AZ 85287-1504

Abstract

Transition metal (TM) fluoride electron beam sensitive resists suitable for the in-situ fabrication of arbitrarily shaped nanometer scale magnetic structures have been developed. 20 nm thick TM fluoride films are prepared by thermal evaporation onto thin carbon films. Nano-patterns are written directly into the TM fluoride film in a scanning transmission electron microscope using a 0.5 nm diameter electron probe. Electron energy loss spectroscopy measurements indicate that as fluorine is released, the TM coalesces. Electron micrographs of exposed patterns show that the resist resolution is on the order of nanometers. Exposure of broad areas leads to coalescent TM layers which cap the remaining fluoride and decrease the rate of fluorine removal. The cross-section for the removal of a fluorine atom and the cross-section for the same process in the presence of an arbitrarily thick capping layer were measured. An electron dose of 1000 C/cm^2 at 100 keV will remove 90% of the fluorine from a 20 nm thick CoF_2 film.

To be published: JUST

Electronic mail: DmitryS@asu.edu; Michael.Scheinfein@asu.edu

DATA QUALITY INSPECTED 4

19971209 073

DISTRIBUTION STATEMENT A

Approved for public release
Distribution Unlimited

Introduction

Recent progress in the experimental study of the growth and characterization of metals on insulators and semiconductors has been motivated by the need to develop smaller integrated semiconductor and magnetic devices. The majority of solid state devices are still fabricated using Si due to the existence of its native oxide, SiO_2 . Direct patterning of electron beam sensitive transition metal halides allows for the creation of nanometer scale magnetic structures at room temperature without chemical processing. This method may facilitate the fabrication of fully integrated electronic and magnetic devices on a single substrate without the deleterious effects of silicide formation. Magnetic sensors, high speed microwave guides, and non-volatile memory are just three of the many applications which may result from constructing solid state devices using transition metals on Si.

Nanometer scale magnetic structures are ideal canonical systems for studying fundamental processes in magnetism. *In-situ* fabrication mediates the effects of oxide formation such that magnetic coupling studies can be performed between structures composed of different shapes over a wide range of length scales. The ability to vary the precise shapes and geometric order of arrays of nanometer size magnetic structures creates opportunities for studying magnetic stability as a function of temperature and externally applied magnetic field.

There are several methods that are employed in the manufacture of small magnetic structures. The most common, optical lithography [1], is a well developed technology that has been widely used. Although optical lithography can provide very high throughput, the smallest size that can be created is limited by diffraction to about $0.2\ \mu\text{m}$. The optical method involves exposure, processing, evaporation and lift-off. Conventional x-ray and electron beam lithography [2-6] increases the resolution of the pattern transfer process to nm length scales, but still requires post processing to remove the resist. The creation of large arrays of small structures can be accomplished

through self-organization [7,8]. This method allows for the fast manufacture of nm structures over large (macroscopic) areas. Although self-organization produces a very rich variety of structures, there is little control over individual particle shapes, ordering in arrays and length scales. Self developing resist x-ray and electron beam lithography [9-11] is a compromise among throughput, resolution and chemical reactivity during processing. The method is very flexible for the *in-situ* manufacture of nano-structures yet the throughput is limited by resist sensitivity and serial processing. However, it is ideally suited for the generation of the small structures needed to examine fundamental magnetic properties at nanometer length scales [7,8]. Na, Li, Mg and Al metal halides self-developing resists [9-11] have been used successfully to prepare nanometer metal structures in an electron microscope. However, there appears to have been no successful attempts at the manufacture of nanometer magnetic structures using direct writing in self-developing resists.

We have tested several transition metal halide compounds for suitability as self-developing resists for the manufacture of magnetic nanostructures. Of the eight transition metal halides tested (FeF_2 , FeF_3 , FeCl_2 , FeCl_3 , CoF_2 , CoF_3 , CoCl_3 and NiF_2) only FeF_2 and CoF_2 are sensitive enough to the electron beam. In this article we report on *in-situ* experiments designed to produce controlled, nanometer sized magnetic structures using FeF_2 and CoF_2 electron beam sensitive resists. The resist properties are characterized using electron energy loss spectroscopy.

Specimen Preparation

The preparation and properties of self-developing FeF_2 and CoF_2 films will ultimately define their utility as the electron beam resists. The thickness of the evaporated film affects both intrinsic properties such as grain size and uniformity as well as extrinsic properties such as the transparency of the resist to the electron beam during the exposure process. Extremely thick (≥ 100 nm) resists are not sufficiently electron transparent to use electron holography [12] for characterization. Thick

films degrade the resolution in the direct write process as they scatter the electron beam strongly [13]. The grain size which increases with increasing film thickness may also limit the ultimate resolution of the patterns transferred with the electron beam. While thin films are easy to write and can have extremely small grains, the coalesced metal structures may not be thick enough to be thermally stable.

Thin FeF_2 and CoF_2 (10-20 nm) films were prepared by thermal evaporation onto a 2-5 nm thick amorphous carbon films in a vacuum of 10^{-8} mBar. Thermal evaporation of metal halides typically requires temperatures in excess of 1000°C [14]. To ensure chemical uniformity of the resists, we use a molybdenum boat which does not form any stable compounds with the resist components. The residual pressure of oxygen and water in the evaporation chamber must be low enough to prevent the halides from decomposing and forming oxides and/or hydrates. The evaporated films have a polycrystalline structure with a crystal grain size ranging from 10 nm to 200 nm. The size of the polycrystals is a strong function of temperature, film thickness and growth rate, ranging from about 10 nm (1 nm/sec) to 100 nm (0.08 nm/sec) for 20 nm thick FeF_2 films grown at room temperature. A growth rate of 1 nm/sec was a practical compromise. The thickness and composition of the films were analyzed using Rutherford Back Scattering.

Both FeF_2 and CoF_2 form anhydrous compounds [15]. CoF_2 has three hydrates: $\text{CoF}_2 \cdot 2\text{H}_2\text{O}$, $\text{CoF}_2 \cdot 3\text{H}_2\text{O}$ and $\text{CoF}_2 \cdot 4\text{H}_2\text{O}$. $\text{CoF}_2 \cdot 4\text{H}_2\text{O}$ decomposes at a temperature of 200°C . It is expected that the other two hydrates decompose in the same temperature range. FeF_2 has two hydrates: $\text{FeF}_2 \cdot 4\text{H}_2\text{O}$ and $\text{FeF}_2 \cdot 8\text{H}_2\text{O}$. These hydrates decompose at 100°C . The presence of water in the halide films degrades both the sensitivity and resolution of the resist. Preheating the evaporant and boat to 200°C in UHV decomposes the hydrates and removes the water. Evaporation was performed at a temperature between 1000 - 1100°C . Although a higher temperature would increase the growth rate

and decrease the polycrystallite size, it could decompose the bulk halide. After evaporation of the film, the specimen must be transferred immediately to the microscope since leaving the halide film exposed to air for ten minutes severely degrades the resist properties.

Experimental investigation of the metal halides properties

Both the nanopatterning and nanocharacterization experiments were performed in a Vacuum Generators HB501 Scanning Transmission Electron Microscope. This microscope is equipped with a Gatan® Parallel Electron Energy Loss Spectrometer (PEELS) and an EmiSpec Vision® computer controlled data acquisition system [16]. Ultimately, this microscope can focus 1 nA of 100 keV electrons into a beam $\frac{1}{2}$ nm in diameter. Digitized patterns were transferred into the halide films by controlling the 100 keV electron beam with a computer while monitoring the electron dose. The computer controlled National Instruments® AT-MIO-16E-2 multichannel digital-to-analog converter can scan the electron beam at rates of up to 400 kHz. Our custom scanning software allows virtually any pattern to be transferred into the resist. Fig. 1 shows a resolution test pattern that has been transferred into the CoF_2 resist. This high resolution annular dark field (ADF) image shows the CoF_2 as gray, and the coalesced Co metal as black. A line scan taken across a single Co line at right has a width (FWHM) of approximately 5 nm. This is not the resolution limit of the resist but rather the linewidth selected for this exposure. There are some proximity effects in lines exposed close to one-another. The boxes at the top of Fig. 1 have incomplete exposure of the lines that comprise the left side of each box. This is because the pattern was written from left to right. The exposed right side of the box immediately to the left of a given box decreased the resist sensitivity local to that exposed line. This proximity effect can be seen in the center of the exposed spoke pattern in the wheel at left in Fig. 1, and as roughness in the smallest lines written close together at the top of the array of lines at the bottom of Fig. 1. In all other cases, the lines are continuous, even and clearly resolved.

The self-development process was qualitatively characterized using bright and dark field imaging, and quantitatively characterized with Electron Energy Loss Spectroscopy (EELS). EELS spectra can provide valuable information in both low loss (0 \rightarrow 100 eV) and high or core loss (100 \rightarrow 1000 eV) energy loss ranges. The low loss EELS spectra can be used to investigate changes in the electronic properties during irradiation. Changes in the composition of the compound during electron irradiation can be determined by monitoring the core loss excitation spectra (scattering cross section) during the electron exposure process. Figs. 2a (2b) illustrate typical EELS spectra for FeF₂ (CoF₂) taken from both exposed and unexposed areas in the energy region surrounding the fluorine K (685 eV) excitation and the Co (779 eV) and Fe (708 eV) L_{2,3} excitations. It is clear from the spectra shown in Fig. 2 that in the exposed areas fluorine was completely removed, while little iron/cobalt mass loss is observed.

We separate the analysis of the self development process in electron beam exposed regions of FeF₂ and CoF₂ into two categories: (a) An electron-beam/resist interaction occurs in exposed areas where F is liberated and the transition metal coalesces. This interaction governs the most basic properties of the resist such as its sensitivity and any thickness dependent effects. (b) In the vicinity of the exposed areas, diffusion of iron/cobalt, redistribution of the halide, and proximity effects due to high angle electron scattering and secondary electron creation reduce the sensitivity of the resist.

The sensitivity of CoF₂ to electron exposure can be measured by monitoring the relative concentrations of Co and F during the irradiation process. Typically, a small region of the sample surface is scanned with the electron beam. The current is monitored as a function of time so that the total electron dose can be established. EELS spectra are accumulated frame by frame as a function of time (dose). One such time series acquired for a 20 nm thick CoF₂ film is shown in Fig. 3. EELS spectra are shown near the F-K and Co-L_{2,3} edges for the five electron doses shown at left. The

relative concentration of F can be determined by fitting ($I = AE^{-1}$) the EELS spectra before the edge ($E < 675$ eV), subtracting this background, and integrating for a fixed energy window under the excitation peak [17]. The relative concentration of F is shown in Fig. 3 at right.

A series of spectra like that shown in Fig. 3 illustrates how the dose response can be extracted from EELS spectra. Using EmiSpec Vision® image acquisition and processing software, such EELS spectra can be collected in real time, the background subtracted, and the suitable energy window integrated, yielding the elemental concentration as a function of dose. The four dose response curves in Fig.4 show both the Co and F concentrations as functions of time (dose) for four different exposed areas, 48×48 nm², 70×70 nm², 140×140 nm² and 190×190 nm² in Figs. 4 a-d respectively. The different size areas were selected in order to explore the dose rate dependence during the exposure process. Each experimental point in Fig.4 indicated by a solid symbol is extracted from an EELS spectrum similar to those shown in Fig.3. The time scale in Fig. 4 was normalized to give a constant current of 100 nA on the condenser aperture (corresponding to 140 pA at the specimen) using a series of current measurements, each taken simultaneously with the EELS spectral series. This procedure is required in order to correct for the beam current instabilities which can be as high as 70% over a period of several minutes. Variations in electron beam current (dose) were also monitored by measuring the area under the carbon K-edge excitation peak in each EELS spectrum. Since each transition metal halide film was deposited on a thin amorphous C substrate, this signal should remain constant in time unless carbon builds up on the specimen during exposure. Bright and dark field STEM images and EELS spectra were inspected both before and after each exposure to ensure that no appreciable carbon buildup occurred.

Expected trends are illustrated in Fig.4. The Co concentration is approximately constant, while the F concentration decreases nearly exponentially. A very simple model of F liberation was

developed in order to explain the observed behavior of the resist under electron beam irradiation as schematically illustrated in Fig. 5. The simplest model of the exposure process is shown in Fig. 5a. Metallic cobalt coalesces only on the exposed region of the surface of the CoF_2 film. A surface layer is expected when the probability of F escape to vacuum is higher close to the surface. It is possible that metallic cobalt forms a continuous surface layer with coalesced clusters with some unknown distribution underneath (Fig. 5b), or even some continuous depth distribution (Fig. 5c). It is possible to measure the Co (metal) depth distribution performing dose response measurements for resists of different thickness. However, since the usable range of film thickness is limited in our application, this was not pursued. Co surface migration can play an important role in defining the resist resolution through proximity effects. This Co migrating along the surface out of an exposed region (Fig. 5d) can be minimized by exposing sufficiently large areas and monitoring Co concentration.

Since the nearly exponential initial decay in F concentration becomes much slower at later stages of exposure (Fig. 4) we postulate that the reduced rate of F escape at higher doses can be explained by the newly coalesced Co metal trapping the F in the layer of CoF_2 that is still unexposed underneath the capping layer (Fig 5a). This is the simplest model (Fig. 5a) to analyze the exposure process. The process can be described by the following differential equation:

$$\frac{dN'_{F(t)}}{dt} = \beta I_e N_{\text{CoF}_2}(t) \exp(-\gamma N_{\text{Co}}(t)). \quad (1)$$

$N'_{F(t)}$ is the areal density (atoms per cm^2) of F escaping from the film, N_{Co} the areal density of the coalescent metallic Co, and N_{CoF_2} the areal density of CoF_2 molecules, β is the ionization cross-section for removing one atom of fluorine from a CoF_2 molecule (if the 100 keV incident beam current density I_e is expressed in electrons/sec/ cm^2), and the exponential factor reflects the potential barrier which traps the F beneath the Co layer, with γ as a measure of the trapping strength, i.e. γ is a

cross-section for one Co atom capping one F atom. The time dependent concentrations of CoF_2 and coalescent metallic Co are given by

$$N_{\text{CoF}_2}(t) = N_0 e^{-t/\tau(t)} \quad N_{\text{Co}}(t) = \frac{N_0}{3} (1 - e^{-t/\tau(t)}) \quad (2)$$

where N_0 is the initial number of atoms in CoF_2 molecules in the unexposed film. The number of atoms of the remaining F (bound in CoF_2) is

$$N_F(t) = \frac{2}{3} N_0 - N'_{\text{F}}(t) = \frac{2}{3} N_{\text{CoF}_2}(t) = \frac{2}{3} N_0 e^{-t/\tau(t)} \quad (3)$$

Note that eqns (2) and (3) are completely general since $\tau=\tau(t)$ is an explicit function of time; the only model dependent equation is eqn (1). Substitution of (2) and (3) into (1) gives the relative concentration of the remaining fluorine $\exp(-t/\tau(t))$ as

$$\frac{d}{dt} e^{-t/\tau(t)} = -\frac{3}{2} \beta I_e \exp(-t/\tau(t)) \exp(-\gamma \frac{N_0}{3} (1 - \exp(-t/\tau(t)))) \quad (4)$$

which cannot be solved in closed form for general $\tau(t)$; solution in a series expansion of t for small t tends to be inaccurate.

The results of fitting eqn. (4) to the experimental data in the Fig.4 with βI_e and γN_0 as unknown parameters for a film of 22 nm nominal thickness, resist density of 4.46 g/cm^3 and electron beam current of 140 pA on the sample are shown in Table 2. σ_F is the ionization cross-section for removing one atom of F by with one 100 keV electron, and σ_{Co} is the capping cross-section defined as probability of capturing one F atom by one Co atom. The decrease in the values of the cross-sections with the increasing exposed area size can be attributed to specimen drift. Errors of such kind are hard to correct since it is not possible to view the image on the microscope screen while the resist is being irradiated. The cross-sections shown in the Table 1 indicate that a 100 keV electron has a 3×10^{-6} chance of ejecting one F atom out when passing through the CoF_2 elementary cell while one

metallic Co atom has a 5×10^{-3} chance of trapping one F atom from the coalescent layer below. The Co trapping cross-section ultimately defines the maximum practically useful thickness of the resist, e.g. for 500 layers of the coalescent cobalt ($\approx 150\text{nm}$) on top of CoF_2 , a F atom has only a 10% chance of escape according to the model used.

The image shown in Fig. 1 suggests that CoF_2 resist resolution is not limited by the polycrystallite size. Unlike some other self-developing electron sensitive resists (e.g. AlF_3) [9], the coalescent metal in CoF_2 and FeF_2 resists does not seem to form clusters. Rather it is distributed uniformly across exposed areas. However, the proximity effect can limit the resist resolution. CoF_2 and FeF_2 may become less sensitive to the electron beam in the vicinity of exposed areas since some transition metal can diffuse out of the locally exposed areas, and cap the resist layers below. EELS spectrum taken from an exposed point (limited by the resist resolution rather than by the electron beam size) shows a somewhat lower concentration of the Fe/Co than a similar spectrum taken from an unexposed area. This loss of the transition metal in extremely small areas supports the explanation that some of the transition metal may spill over onto adjacent areas during exposure.

In order to try to quantify the length scales for Co migration during the exposure/capping process, we exposed a series of the rectangular regions with the same area but varying aspect ratio. It is intuitively clear that rectangles with a higher aspect ratio will have more Co diffusing out since the perimeter/area ratio is larger and hence there is a higher probability for a Co atom to escape the exposure region. In the crudest approximation, this process can be thought of as simple diffusion with a Gaussian distribution of the distances traveled by Co atoms and the diffusion distance independent on whether atom travels across an exposed or unexposed area. An expression for the Co concentration in the exposed region can be calculated by convoluting a Gaussian distribution with an initial concentration of the free Co, which is 1 for a point inside an exposed region and 0 otherwise. Fig. 6 shows a simulation of the relative Co concentration as a function of the aspect ratio for 5

different diffusion distances (1, 2, 4, 8 and 16 nm) and an area of 5000 nm². The experimental data for the rectangles with the aspect ratios of 1, 2, 4, 8, 16, 32 and 64 with the exposed area of 5000 nm² are superimposed on Fig. 6. Even though the experimental data can serve only as a qualitative measure, it allows us to estimate an upper limit for the diffusion distance as $\sigma \leq 4$ nm, which is consistent with the proximity effect in the experimental image in Fig. 1.

Conclusions

We have demonstrated that new high resolution electron beam sensitive FeF₂ and CoF₂ resists can be vacuum sublimated and used for the *in-situ* manufacture of small magnetic structures. Measured sensitivity, capping and proximity effects show that it is feasible to use those resists for the manufacturing of the arbitrary shaped magnetic structures with the linear size of 10 nm and a thickness of 100 nm or less. The lower limit on the size of the manufactured magnetic structure is set by the resists resolution. While the resist sensitivity is lower than that for traditional electron beam resists, electron microscope images can still be obtained in a conventional electron microscope with the beam current on the order of 1 nA.

Acknowledgments

We are indebted to Dr. G. Hembree for collaboration and assistance. We thank A. Higgs and J. Wheatley for providing electron microscope support. This work was supported by the ONR 00014-95-1-0891. The microscopy was performed in the Center for High-Resolution Microscopy at Arizona State University supported by NSF DMR93-14326.

References

- [1] W. Van Roy, E. L. Carpi, M. Van Hove, A. Van Esch, R. Bogaerts, J. De Boeck and G. Borghs,

- J. Magn. Magn. Mater., **121**, 197 (1993).
- [2] P. R. Krauss and S. Y. Chou, J. Vac. Sci. Technol. **B13**, 2850, (1995).
- [3] S. McVitie and J. N. Chapman, IEEE MAG-24, 1778, (1988).
- [4] J. F. Smyth, S. Schultz, D. Kern, H. Schmid and Dennis Yea, J. Appl. Phys., **63**, 4237, (1988).
- [5] S. J. Hefferman, J. N. Chapman, S. McVitie, J. Magn. Magn. Mater., **95**, 76, (1991).
- [6] A. B. Johnston, J. N. Chapman, B. Khansehpour and C. D. W. Wilkinson, J. Phys., **29**, 1419, (1996).
- [7] A. Sugawara, T. Coyle, G. G. Hembree and M. R. Scheinfein, Appl. Phys. Lett., **70**, 1043, (1997).
- [8] A. Sugawara and M. R. Scheinfein, Phys. Rev. **B56**, in-press, (1997).
- [9] A. Muray, M. Scheinfein, M. Isaacson, J. Vac. Sci. Technol. **B3**, 367, (1985).
- [10] Qun Dou, D. W. Lynch, Surf. Sci. **219**, 623, (1989).
- [11] Heiji Watanabe, Jun-ichi Fujita, Yukinori Ochiai, Shinji Matsui and Masakazu Ichikawa, Jpn. J. Appl. Phys., **34**, 6950, (1995).
- [12] A. Tonamura, *Electron Holography* (Springer Verlag, Berlin, 1993).
- [13] L. Reimer, *Transmission Electron Microscopy* (Springer Verlag, Berlin, 1993).
- [14] R. D. Mathis Company, *Thin film evaporation source reference* (Lebow Co, Goletta, 1987).

[15] R. C. Weast (Ed.), *CRC Handbook of Chemistry and Physics* (CRC Press, Boca Raton, 1980).

[16] Thanks to scientists at EmiSpec Corporation for help with custom data acquisition and control software.

[17] R.F. Egerton, *Electron Energy Loss Spectroscopy in the Electron Microscope* (Plenum Press, New York, 1986).

Figure Captions

Fig. 1 : High angle annular dark field image of a resolution test pattern transferred into CoF_2 using 100 keV electrons in STEM. The gray areas are CoF_2 , the black areas are metallic Co. The resolution here is limited by the scan rather than the resist to about 5 nm. Proximity resist effects can be observed (see text).

Fig. 2 : Electron energy loss spectra in the energy region surrounding the fluorine K-edge (685 eV), the Co (779 eV) and Fe (708 eV) $L_{2,3}$ excitations for (a) FeF_2 and (b) CoF_2 before and after electron beam irradiation.

Fig. 3 : Dose response EELS spectra in the core excitation region for CoF_2 . The decrease in the F K-edge intensity near 690 eV energy loss is evident as a function of the dose indicated at left. The relative F concentration is shown at right.

Fig. 4 : Dose response curves for CoF_2 show both the relative Co and F concentrations as the functions of time (dose) for four different exposed areas, (a) $48 \times 48 \text{ nm}^2$, (b) $70 \times 70 \text{ nm}^2$, (c) $140 \times 140 \text{ nm}^2$ and (d) $190 \times 190 \text{ nm}^2$. The different size areas were selected in order to explore the dose rate dependence in the exposure process.

Fig. 5 : Simple models for exposure include in order of increasing complexity (a) a simple capping layer; (b) simple capping layer with volume exposed regions; (c) continuous distribution of metallic

Co and (d) the addition of Co diffusing out of the exposed region.

Fig. 6 : Relative Co concentration as a function of the aspect ratio for 5 different diffusion distances (1, 2, 4, 8 and 16 nm) and an area of 5000 nm². The experimental data are superimposed and indicated by solid symbols.

Table Captions

Table 1 : Dose Response Model Parameters for CoF₂.

Tables

Table 1: Dose Response Model Parameters for CoF₂

Figure #	area nm ²	βI_e	γN_0	$\sigma_F, 10^{-20} \text{ cm}^2$	$\sigma_{Co}, 10^{-20} \text{ cm}^2$
Fig.4a	48 x 48	0.1 ± 0.03	14 ± 3	0.25 ± 0.1	750 ± 200
Fig.4b	70 x 70	0.04 ± 0.01	11 ± 3	0.23 ± 0.07	600 ± 200
Fig.4c	140 x 140	0.005 ± 0.002	12 ± 3	0.11 ± 0.04	650 ± 200
Fig.4d	190 x 190	0.0007 ± 0.0002	2 ± 0.5	0.03 ± 0.01	100 ± 300

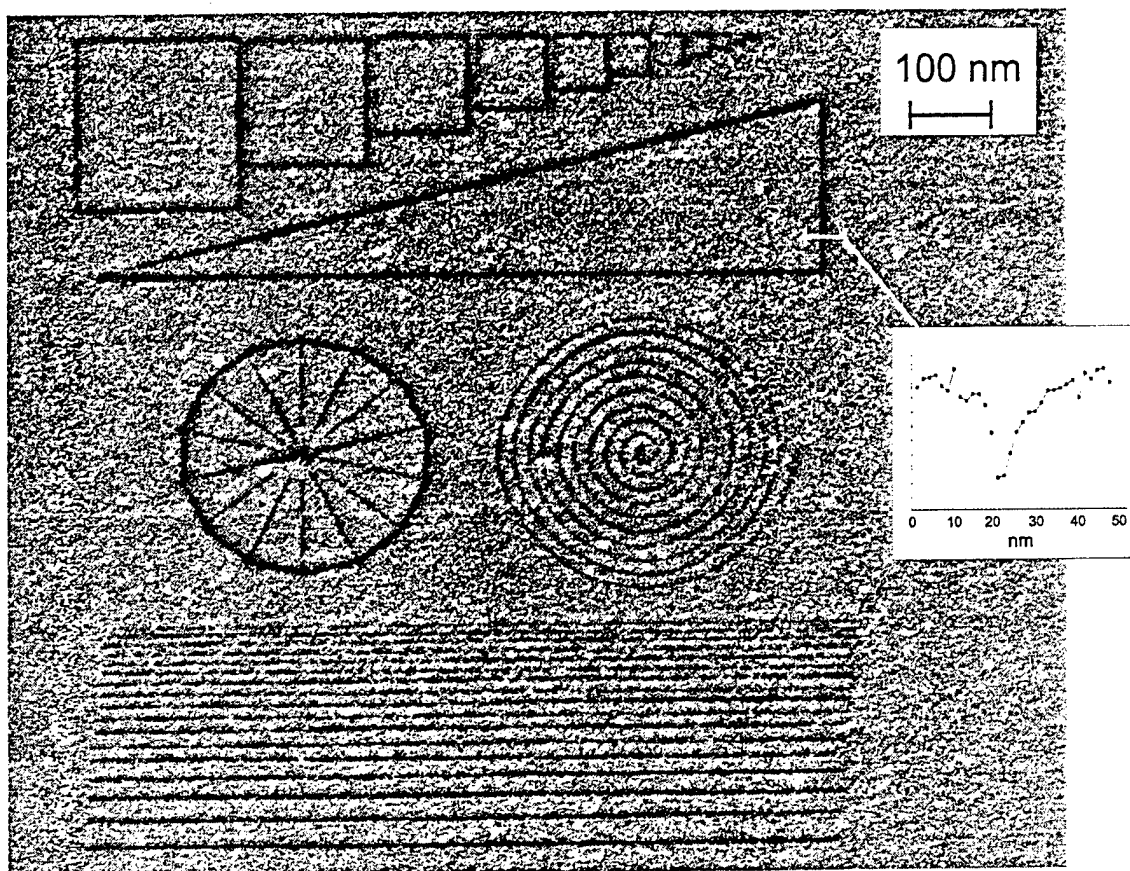


Figure # 1.

Dmitry Streblechenko, M. R. Scheinfein

JVST

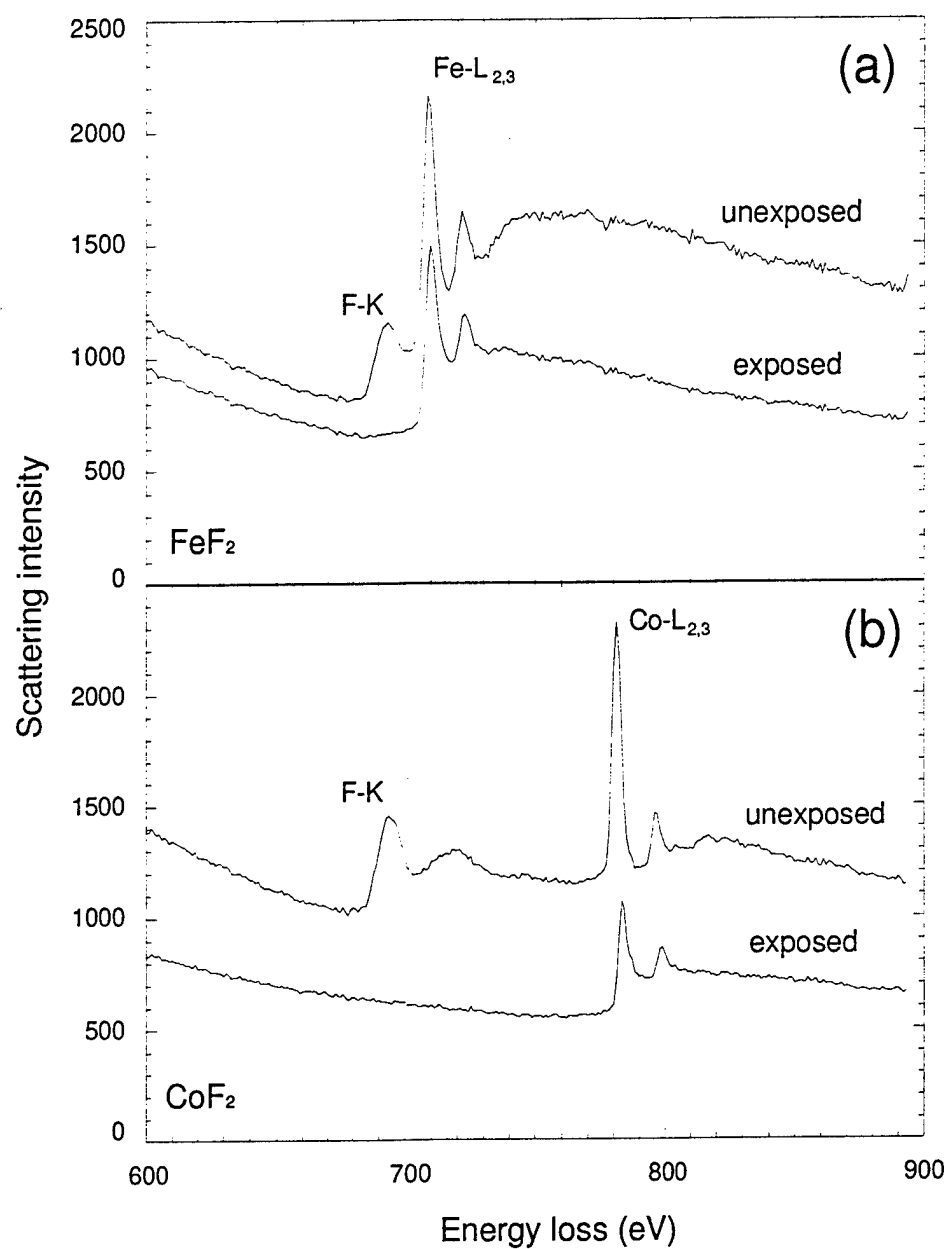


Figure # 2.

Dmitry Streblechenko, M. R. Scheinfein

JVST

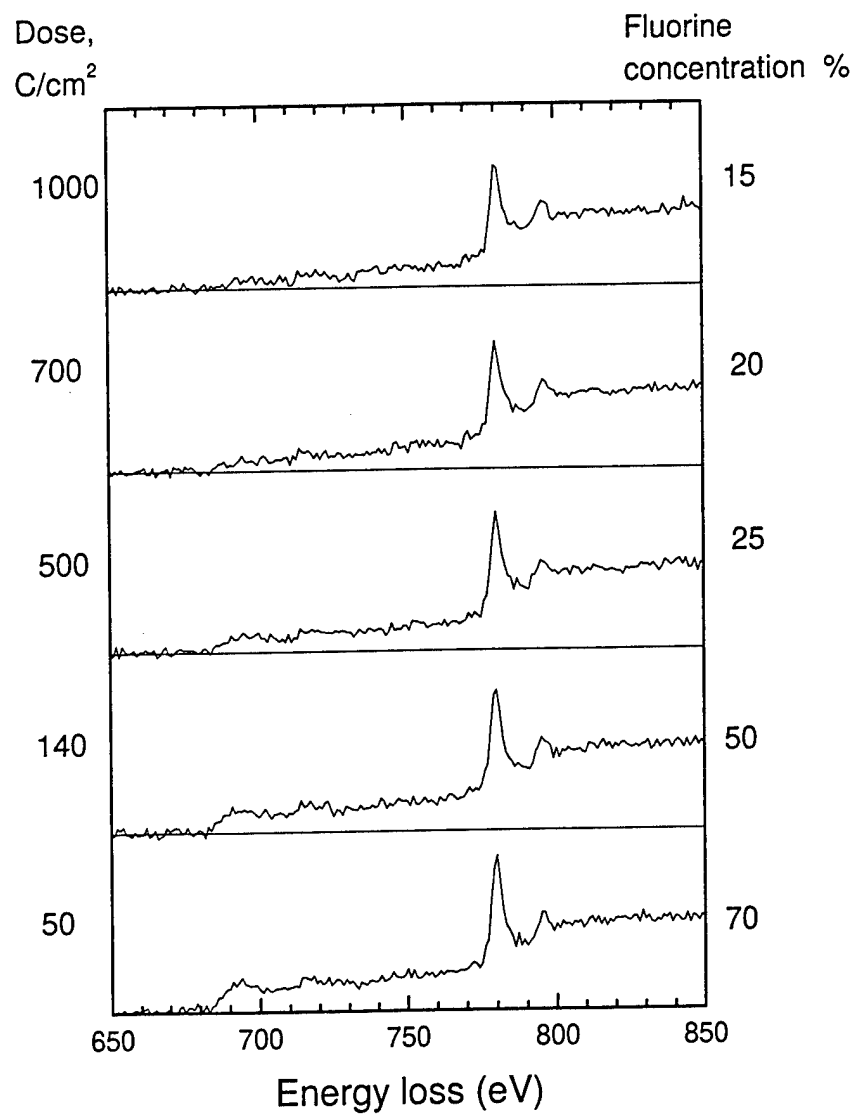


Figure # 3.

Dmitry Streblechenko, M. R. Scheinfein

JVST

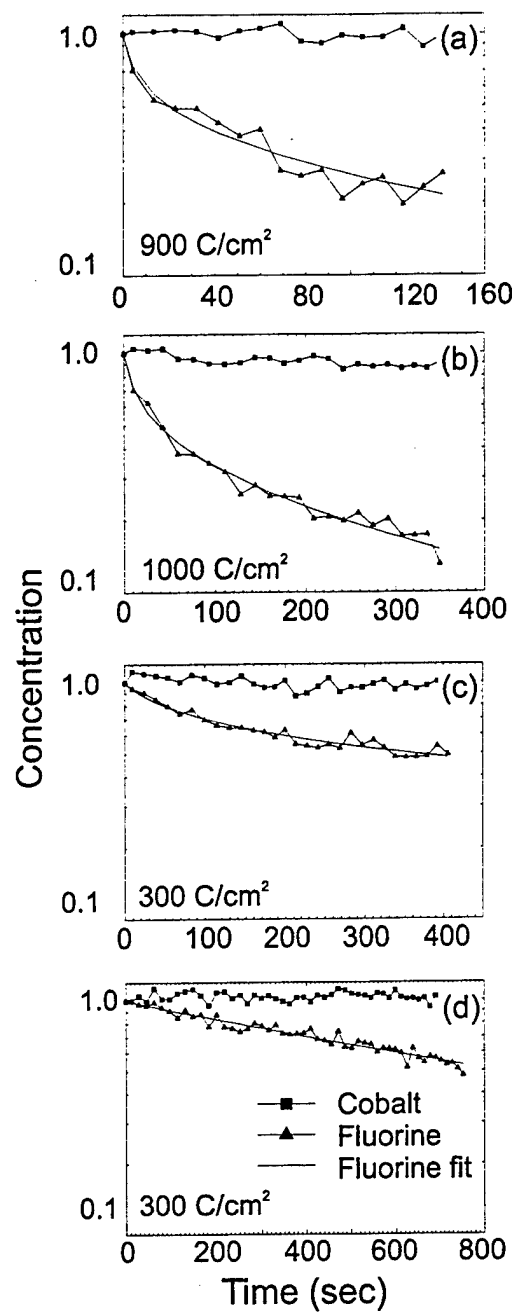


Figure # 4.

Dmitry Streblechenko, M. R. Scheinfein

JVST

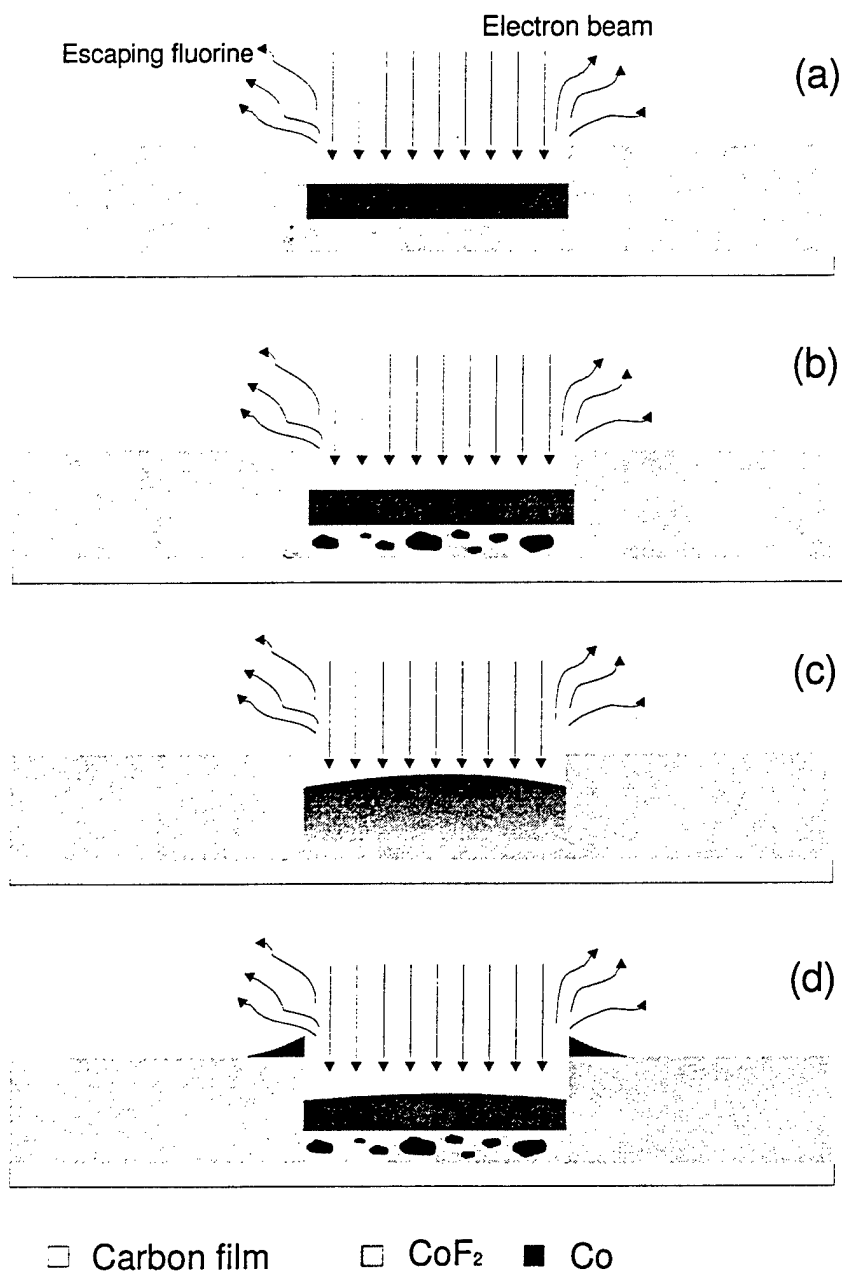


Figure # 5.

Dmitry Streblechenko, M. R. Scheinfein

JVST

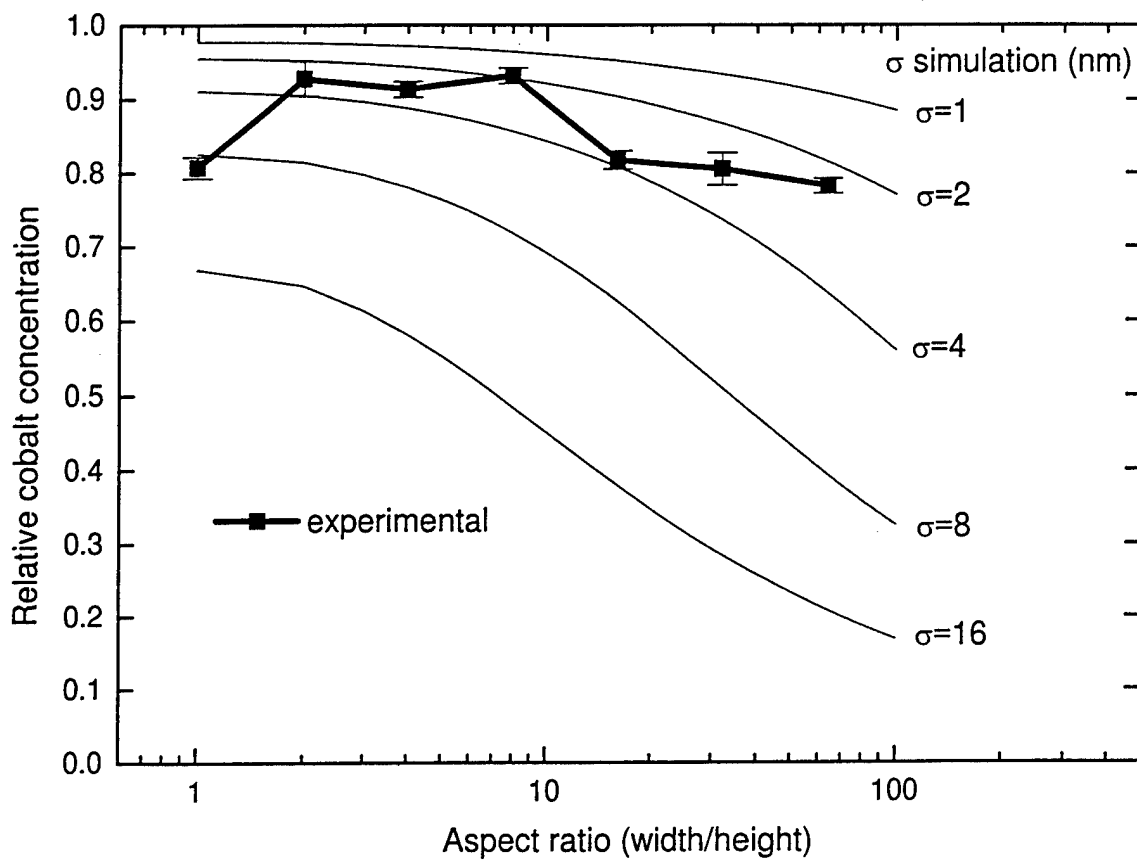


Figure # 6.

Dmitry Streblechenko, M. R. Scheinfein

JVST